

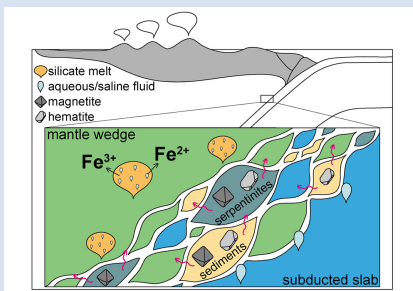
■ Preferential mobilisation of oxidised iron by slab-derived hydrous silicate melts

C. Tiraboschi^{1*}, C. McCammon², A. Rohrbach¹, S. Klemme¹, J. Berndt¹, C. Sanchez-Valle¹



<https://doi.org/10.7185/geochemlet.2304>

Abstract



The role of slab-derived hydrous silicate melts in the transfer of the oxidised signature in subduction zones remains poorly constrained. We have investigated the mobility and redox state of iron in hydrous silicate melts by carrying out solubility measurements of hematite–magnetite assemblages in a piston–cylinder apparatus combined with electron microprobe and Mössbauer analysis of the recovered glasses. The experiments were performed at subcritical conditions, *i.e.* two-fluid phases coexisting with the solid assemblage. We observe concentrations of total FeO as high as 1.85 ± 0.18 wt. % (2.07 ± 0.41 wt. % in saline systems) at 2 GPa and 900 °C, with $\text{Fe}^{3+}/\text{Fe}_{\text{tot}}$ ratios of 0.79 ± 0.04 (0.45 ± 0.07) that indicate the dominance of oxidised iron in the melt phase. Combined with thermodynamic modelling to reconstruct the composition and speciation of the coexisting fluid phase, we demonstrate that hydrous silicate melts can transport 20 times more dissolved iron, preferentially as oxidised iron, than aqueous fluids at sub-arc conditions. Our results support the efficient dissolution of ‘fluid-insoluble’ iron oxides in slab-melts, which are thus efficient agents for the transfer of oxidised iron to the mantle wedge, ultimately contributing to the oxidation of the arc magma source.

Received 18 August 2022 | Accepted 28 December 2022 | Published 31 January 2023

Introduction

Arc magmas are characterised by a higher oxidation degree than magmas from other tectonic settings, including mid-oceanic ridge and ocean arc basalts (Carmichael, 1991; Kelley and Cottrell, 2009; Brounce *et al.*, 2014). The oxidised signature is thought to arise from the influx of oxidising slab-derived fluids or melts into the mantle wedge (*e.g.*, Burgisser and Scaillet, 2007; Debret and Sverjensky, 2017; Bénard *et al.*, 2018; Walters *et al.*, 2020; Evans and Frost, 2021), although the actual oxidising agent and the transport mechanism remain a topic of discussion (*e.g.*, Piccoli *et al.*, 2019; Tollan and Hermann, 2019). Iron, as the most abundant redox-sensitive element in the upper mantle, may play a pivotal role in these processes, and constraints on its mobility and speciation in slab-derived phases are thus critical to elucidating the range of redox state conditions of subduction zones (Frost and McCammon, 2008; Kelley and Cottrell, 2009; Evans, 2012).

Iron oxides such as hematite, Fe_2O_3 , and magnetite, Fe_3O_4 , are by-products of serpentinisation (*e.g.*, Carboni *et al.*, 2015; Debret *et al.*, 2015), and they have been identified in sea-floor metasediments (*e.g.*, Ague *et al.*, 2022). Consequently, their solubility may control the iron budget in slab-derived fluids and melts. To date, most experimental studies on the solubility of hematite and/or magnetite in aqueous fluids (Chou and Eugster, 1977; Boctor *et al.*, 1980; Frantz *et al.*, 1981; Scholten *et al.*, 2019) and melts (Simon *et al.*, 2004; Bell and Webster,

2015), have been conducted at moderate pressures, less than 0.4 GPa, that are not relevant for sub-arc settings. A single study of hematite solubility in H_2O –NaCl fluid at 1 GPa and 800 °C by Wykes *et al.* (2008) reported dissolved iron contents below 0.01 mol/kg. This value implies Fe^{3+} fluxes of 10^9 mol/year, which are three to four orders of magnitude lower than the estimated redox budget flux ($55 \pm 13 \times 10^{12}$ mol/year; Evans, 2012). Alternatively, silica-bearing melt-like fluids have been suggested as an efficient agent for the transfer of oxidised iron (Parkinson and Arculus, 1999; Hermann *et al.*, 2006; Kelley and Cottrell, 2009; Bénard *et al.*, 2018) owing to its low solubility in aqueous phases (Wykes *et al.*, 2008). Yet, the capacity of hydrous silicate melts to transport oxidised iron at sub-arc conditions remains unconstrained.

Here, we present experimental data on the solubility of hematite–magnetite assemblages in hydrous haplogranitic melts, which mimic melts produced by partial melting of subducted metasediments, to constrain their ability to transfer oxidised iron at sub-arc conditions. Combined with Mössbauer spectroscopy analysis of the recovered glasses and thermodynamic modelling, we demonstrate the higher capacity of hydrous silicate melts to mobilise oxidised iron compared to aqueous and chlorinated fluids at sub-arc conditions. The dissolution of iron oxides in slab-derived silicate melts thus provides a viable mechanism for the transfer of oxidised iron from the slab to the mantle wedge and to explain the oxidised nature of arc magmas (Kelley and Cottrell, 2009).

1. Institut für Mineralogie, Westfälische Wilhelms-Universität Münster, 48149 Münster, Germany

2. Bayerisches Geoinstitut, Universität Bayreuth, 95440 Bayreuth, Germany

* Corresponding author (email: ctirabos@uni-muenster.de)



Solubility and Redox State of Iron in Hydrous Silicate Melts

A total of 16 hematite–magnetite solubility experiments were performed at 1–2 GPa and 700–950 °C (Fig. 1, Table 1, Fig. S-1, and Table S-1). Experimental and analytical details can be found in the [Supplementary Information](#).

Measured FeO contents in the quenched glasses from the H₂O + melt system (Fig. 2a) range from 0.60 ± 0.21 wt. % at 1 GPa and 700 °C to 1.96 ± 0.04 wt. % at 1 GPa and 950 °C. In the H₂O–NaCl + melt system (Fig. 2b), the FeO content increases from 0.75 ± 0.08 wt. % at 1 GPa and 700 °C to 2.40 ± 0.12 wt. % at 1 GPa and 950 °C. Within error, similar FeO contents were measured in glasses quenched at 2 GPa in both pure H₂O and saline systems. Hence there is no significant pressure effect on iron solubility in agreement with previous low-pressure experiments in melt-free HCl-bearing fluids (Scholten *et al.*, 2019). The two experimental runs performed with either magnetite or hematite in the presence of a hydrous melt phase displayed lower FeO contents in the quenched glass at 1 GPa and 900 °C compared to experiments in which both oxides were present, *i.e.* 1.61 ± 0.09 wt. % and 1.42 ± 0.13 wt. %, respectively (Fig. 2a). The FeO contents reported here compare well with the results from sediment melting experiments at similar conditions (*e.g.*, Hermann and Spandler, 2008) and from natural melt inclusions in hematite–magnetite-bearing mantle xenoliths (*e.g.*, Blatter and Carmichael, 1998). A more detailed comparison is provided in the [Supplementary Information](#).

Mössbauer absorption spectra recorded on selected re-covered glasses (*i.e.* with the highest FeO content) yielded Fe³⁺/Fe_{tot} ratios of 0.79 ± 0.04 in the H₂O + haplogranite melt system (Fig. S-2a), while a lower Fe³⁺/Fe_{tot} ratio of 0.45 ± 0.07 was retrieved in the H₂O–NaCl + melt system (Fig. S-2b), both at 2 GPa and 900 °C. Unbuffered experiments at 1 GPa and 900 °C showed Fe³⁺/Fe_{tot} ratios of 0.64 ± 0.15 and 0.73 ± 0.22 for the magnetite-only and hematite-only experiments, respectively (Fig. S-2c and S-2d). Additional details about the coordination environment of Fe³⁺ in the melt structure and the two unbuffered experimental runs are discussed in the [Supplementary Information](#) (Fig. S-2, S-3, and Table S-2).

Aqueous Fluids vs. Hydrous Silicate Melts as Carriers of Oxidised Iron

We show that significant amounts of iron, preferentially as Fe³⁺, can be mobilised and transported by hydrous silicate melts at sub-arc conditions. To compare the relative iron transport capacity of aqueous fluids and hydrous silicate melts, we further performed equilibrium thermodynamic calculations using the DEW model (Sverjensky *et al.*, 2014) and computed the iron content (and speciation) in the aqueous phase at run conditions (see [Supplementary Information](#)).

Thermodynamic modelling results indicate that hematite and magnetite are insoluble in H₂O-only fluids at the investigated *P*, *T*, and *f*O₂ conditions (Table S-3), with iron concentrations that are several orders of magnitude lower than those measured in the quenched glass (Fig. 3a). However, the stepwise addition of silica as Si(OH)₄, following the haplogranite melt dissolution into the fluid, significantly increases the FeO content compared to the H₂O-only system, due to the formation of a hydrous Fe–Si complex with stoichiometry Fe(H₃SiO₄)⁺ (Fig. 3a). Dissolved silicate species (Manning *et al.*, 2010) thus provide additional ligands that enhance the mobilisation and transport of iron as previously reported for other ‘immobile’ metals, such as Zr, Ti, Nb (Audétat and Keppler, 2005; Manning *et al.*, 2008; Wilke *et al.*, 2012; Louvel *et al.*, 2013) and most recently, for carbon in graphite-saturated systems (Tiraboschi *et al.*, 2022 and references therein). In H₂O–NaCl fluids, in contrast, the formation of FeCl₂ complexes yields iron concentrations in the fluid in equilibrium with hematite–magnetite that are 4 orders of magnitude higher than in pure H₂O (Fig. 3b and Table S-3). The addition of dissolved silica in the model further enhances the solubility of iron *via* the formation of Fe(H₃SiO₄)⁺ species that, together with Cl-complexes, lead to concentrations of Fe²⁺ dissolved in the fluid that are up to 5 times higher compared to the NaCl-free system.

In both H₂O and H₂O–NaCl systems, the calculated FeO solute content in the fluid is 1 order of magnitude lower than in quenched glasses, hence indicating a higher iron transport capacity of melt compared to aqueous and saline fluids. Moreover, the Mössbauer data indicate that the higher FeO content in the quenched glass is mainly due to the presence of oxidised iron that dominates in the melt phase (Table 1 and Fig. 3).

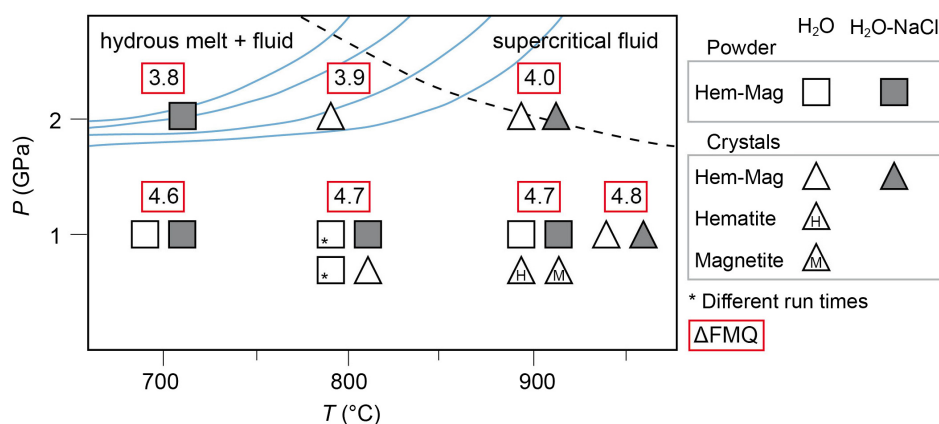


Figure 1 Pressure and temperature conditions of experimental runs employing powders (squares) or single crystals (triangles) as starting materials. The oxygen fugacity is reported relative to the Fayalite–Magnetite–Quartz (FMQ) buffer. The dotted line denotes the critical curve in the haplogranite–H₂O system (Bureau and Keppler, 1999). Solid lines represent hot subduction geothermal paths (Syracuse *et al.*, 2010).

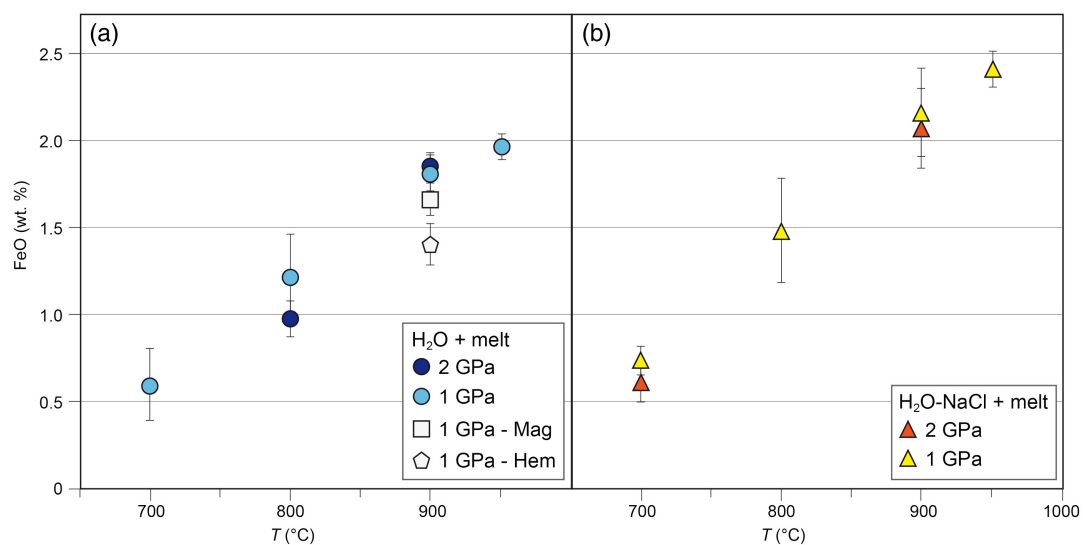
Table 1 Experimental run conditions, FeO content (in wt. %) and Fe³⁺/Fe_{tot} ratios in the quenched haplogranite glasses as determined by EMPA and Mössbauer spectroscopy, respectively.

Run no.	P (GPa)	T (°C)	Run duration	Starting fluid	FeO (wt. %)	logfO ₂ (bar)	ΔFMQ [#]	Fe ³⁺ /Fe _{tot}
GHM3	1	700	48	H ₂ O	0.60 (0.21)	-11.5	4.6	
GHM6	1	700	48	H ₂ O-NaCl	0.75 (0.08)	-11.5	4.6	
GHM1	1	800	24	H ₂ O	1.04 (0.12)	-9.0	4.7	
GHM5	1	800	72	H ₂ O	1.22 (0.24)	-9.0	4.7	
GHM2*	1	800	72	H ₂ O	1.23 (0.06)	-9.0	4.7	
GHM7	1	800	24	H ₂ O-NaCl	1.50 (0.31)	-9.0	4.7	
GHM4	1	900	24	H ₂ O	1.82 (0.11)	-7.1	4.7	
GHM11	1	900	24	H ₂ O-NaCl	2.17 (0.26)	-7.1	4.7	
GM1*	1	900	24	H ₂ O	1.61 (0.09)	-	-	0.64 ± 0.15
GH2*	1	900	24	H ₂ O	1.42 (0.13)	-	-	0.73 ± 0.22
GHM13*	1	950	24	H ₂ O	1.96 (0.04)	-6.4	4.8	
GHM15*	1	950	24	H ₂ O-NaCl	2.40 (0.12)	-6.4	4.8	
GHM19	2	700	48	H ₂ O-NaCl	0.60 (0.09)	-11.3	3.8	
GHM20*	2	800	24	H ₂ O	0.96 (0.11)	-8.9	3.9	
GHM9*	2	900	24	H ₂ O	1.85 (0.18)	-6.9	4.0	0.79 ± 0.04
GHM10*	2	900	24	H ₂ O-NaCl	2.07 (0.41)	-6.9	4.0	0.45 ± 0.07

Notes: [#]ΔFMQ = logfO₂^{run} - logfO₂^{FMQ} (Fayalite+Magnetite+Quartz).

*Runs employing single crystals as starting materials. GM1 and GH2 denote runs with only magnetite or hematite (unbuffered conditions).

Uncertainties (in parenthesis) given as 1 standard deviation of *n* (10 < *n* < 50) EMP analyses of the glass.

**Figure 2** Experimental FeO contents (wt. %) measured by EMPA in the quenched glasses, as a function of temperature for (a) the H₂O + melt system and (b) the H₂O-NaCl + melt system.

Taking into account the total FeO content obtained by EMP analyses (Table 1 and Table S-1) and the Mössbauer Fe³⁺/Fe_{tot} ratio, the estimated Fe₂O₃ content in the quenched glasses corresponds to 1.59 wt. % and 0.98 wt. % for the pure H₂O and H₂O-NaCl systems, respectively. The lower Fe₂O₃ content in the saline system can be partially attributed to the higher abundance of Fe²⁺, due to the higher solubility of hematite and magnetite in H₂O-NaCl fluids (*i.e.* 0.118 mol/kg), *i.e.* two times the calculated solubility in the H₂O-only system (0.057 mol/kg).

Mobilisation and Transfer of Oxidised Iron at Sub-Arc Conditions

Our experimental results show that hematite and magnetite can be effectively dissolved by hydrous silicate melts and provide the

first constraints of the amount of oxidised iron transferred by hydrous melts at sub-arc conditions. As the Fe³⁺/Fe_{tot} ratio in silicate melts increases upon increasing temperature and oxygen fugacity (Wilke *et al.*, 2002; Borisov and McCammon, 2010; Mysen and Richet, 2019), our results at 2 GPa and 900 °C (0.98–1.59 wt. % Fe₂O₃) likely represent the upper limit for Fe³⁺ transferred by hydrous melts as the temperature is higher than typical conditions for most hot subduction regimes (Fig. 1). Applying correlations between the Fe³⁺/Fe²⁺ ratio and the oxygen fugacity (see details in the Supplementary Information, Fig. S-4), we estimate the Fe₂O₃ content in hydrous silicate melts at sub-arc conditions in hot subduction slabs, *i.e.* 2 GPa and 700 °C (Fig. 1), to be 0.15–0.23 wt. % and 0.05–0.08 wt. % for pure H₂O and saline systems, respectively. The amount of oxidised iron mobilised by the dissolution of hematite–magnetite assemblages in hydrous melts ranges between 0.15

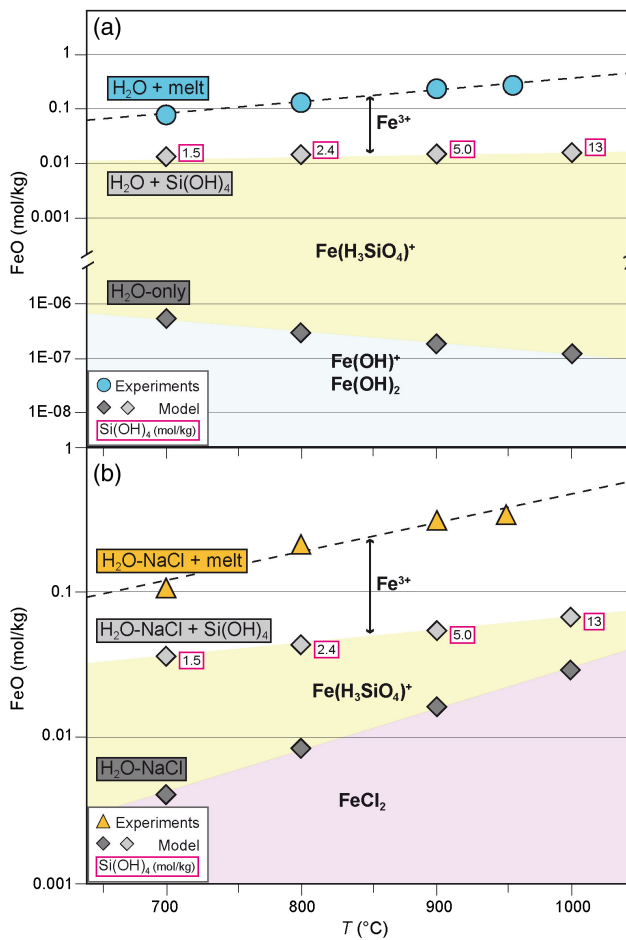


Figure 3 Calculated hematite–magnetite solubility (DEW model, Sverjensky *et al.*, 2014) in (a) aqueous and (b) saline fluids at 1 GPa, and comparison with experimental results in silicate melts. Dark grey diamonds: FeO content (mol/kg) in the H₂O-only and H₂O-NaCl system. Light grey diamonds: FeO (mol/kg) in Si(OH)₄-bearing fluids (mol/kg, pink boxes). Circles (H₂O-only) and triangles (H₂O-NaCl) denote experimental FeO contents in hydrous silicate melts (mol/kg) from this study. Error bars are smaller than the symbol size. The black double-headed arrow shows the effect of oxidised iron. Coloured fields denote the dominance of the indicated solute species in the fluid.

to 1.59 wt. % (0.05 to 0.98 wt. % in saline systems) Fe₂O₃ for the range of hot subduction slab geotherms. The dissolution of ‘fluid-insoluble’ iron oxides in hydrous slab-melts may thus have a significant contribution to the iron budget and redox capacity of the slab flux and should be considered when estimating the redox state of hot subduction zones.

Despite the simplicity of the system investigated here, our results have direct implications for subduction environments where melting of hematite and magnetite-bearing metasediments occur (Ague *et al.*, 2022) or where hydrous silicate melts produced by metasediment slices interact with serpentine in subduction mélanges (Marschall and Schumacher, 2012). Hydrous silicate melts are thus efficient agents for the mobilisation and transfer of oxidised iron from the slab to the mantle wedge, ultimately contributing to the oxidation of the arc magma source.

Acknowledgements

This work was supported by the German Research Foundation (DFG) through grants TI 1078/2-1 and SA 2585/4-1. C.T.

acknowledges a mobility grant from the Italian Society of Mineralogy and Petrography (SIMP). S. Flietakis and Z. Liu are thanked for their assistance in the laboratory, M. Trogisch and B. Schmitte for sample preparation, and D. Sverjensky and S. Tumati for help with the thermodynamic modelling. Katy Evans and Antoine Bénard are acknowledged for helpful reviews and Horst Marschall for editorial handling.

Editor: Horst R. Marschall

Additional Information

Supplementary Information accompanies this letter at <https://www.geochemicalperspectivesletters.org/article2304>.



© 2023 The Authors. This work is distributed under the Creative Commons Attribution Non-Commercial No-Derivatives 4.0

License, which permits unrestricted distribution provided the original author and source are credited. The material may not be adapted (remixed, transformed or built upon) or used for commercial purposes without written permission from the author. Additional information is available at <https://www.geochemicalperspectivesletters.org/copyright-and-permissions>.

Cite this letter as: Tiraboschi, C., McCammon, C., Rohrbach, A., Klemme, S., Berndt, J., Sanchez-Valle, C. (2023) Preferential mobilisation of oxidised iron by slab-derived hydrous silicate melts. *Geochem. Persp. Let.* 24, 43–47. <https://doi.org/10.7185/geochemlet.2304>

References

- AGUE, J.J., TASSARA, S., HOLYCROSS, M.E., LI, J.-L., COTTRELL, E., SCHWARZENBACH, E.M., FASSOULAS, C., JOHN, T. (2022) Slab-derived devolatilization fluids oxidized by subducted metasedimentary rocks. *Nature Geoscience* 15, 320–326. <https://doi.org/10.1038/s41561-022-00904-7>
- AUDÉTAT, A., KEPPLER, H. (2005) Solubility of rutile in subduction zone fluids, as determined by experiments in the hydrothermal diamond anvil cell. *Earth and Planetary Science Letters* 232, 393–402. <https://doi.org/10.1016/j.epsl.2005.01.028>
- BELL, A.S., WEBSTER, J.D. (2015) Dissolved Cl, oxygen fugacity, and their effects on Fe behavior in a hydrous rhyodacitic melt. *American Mineralogist* 100, 1595–1599. <https://doi.org/10.2138/am-2015-5197>
- BÉNARD, A., KLIMM, K., WOODLAND, A.B., ARCULUS, R.J., WILKE, M., BOTCHARNIKOV, R.E., SHIMIZU, N., NEBEL, O., RIVARD, C., IONOV, D.A. (2018) Oxidising agents in sub-arc mantle melts link slab devolatilisation and arc magmas. *Nature Communications* 9, 1–10. <https://doi.org/10.1038/s41467-018-05804-2>
- BLATTER, D.L., CARMICHAEL, I.S.E. (1998) Hornblende peridotite xenoliths from central Mexico reveal the highly oxidized nature of subarc upper mantle. *Geology* 26, 1035–1038. [https://doi.org/10.1130/0091-7613\(1998\)026%3C1035:HPXFCM%3E2.3.CO;2](https://doi.org/10.1130/0091-7613(1998)026%3C1035:HPXFCM%3E2.3.CO;2)
- BOCTOR, N.Z., POPP, R.K., FRANTZ, J.D. (1980) Mineral-solution equilibria—IV. Solubilities and the thermodynamic properties of FeCl₂⁰ in the system Fe₂O₃–H₂–H₂O–HCl. *Geochimica et Cosmochimica Acta* 44, 1509–1518. [https://doi.org/10.1016/0016-7037\(80\)90115-5](https://doi.org/10.1016/0016-7037(80)90115-5)
- BORISOV, A., MCCAMMON, C. (2010) The effect of silica on ferric/ferrous ratio in silicate melts: An experimental study using Mössbauer spectroscopy. *American Mineralogist* 95, 545–555. <https://doi.org/10.2138/am.2010.3217>
- BROUNCE, M.N., KELLEY, K.A., COTTRELL, E. (2014) Variations in Fe³⁺/ΣFe of Mariana Arc Basalts and Mantle Wedge fO₂. *Journal of Petrology* 55, 2514–2536. <https://doi.org/10.1093/ptrology/egu065>
- BUREAU, H., KEPPLER, H. (1999) Complete miscibility between silicate melts and hydrous fluids in the upper mantle: Experimental evidence and geochemical implications. *Earth and Planetary Science Letters* 165, 187–196. [https://doi.org/10.1016/S0012-821X\(98\)00266-0](https://doi.org/10.1016/S0012-821X(98)00266-0)
- BURGISSER, A., SCAILLET, B. (2007) Redox evolution of a degassing magma rising to the surface. *Nature* 445, 194–197. <https://doi.org/10.1038/nature05509>



- CARBONIN, S., MARTIN, S., TUMIATI, S., ROSSETTI, P. (2015) Magnetite from the Cogne serpentinites (Piemonte ophiolite nappe, Italy). Insights into seafloor fluid–rock interaction. *European Journal of Mineralogy* 27, 31–50. <https://doi.org/10.1127/ejm/2014/0026-2410>
- CARMICHAEL, I.S.E. (1991) The redox states of basic and silicic magmas: a reflection of their source regions? *Contributions to Mineralogy and Petrology* 106, 129–141. <https://doi.org/10.1007/BF00306429>
- CHOU, I.M., EUGSTER, H.P. (1977) Solubility of magnetite in supercritical chloride solutions. *American Journal of Science* 277, 1296–1314. <https://doi.org/10.2475/ajs.277.10.1296>
- DEBRET, B., SVERJENSKY, D.A. (2017) Highly oxidising fluids generated during serpentinite breakdown in subduction zones. *Scientific Reports* 7, 1–6. <https://doi.org/10.1038/s41598-017-09626-y>
- DEBRET, B., BOLFAN-CASANOVA, N., PADRON-NAVARTA, J.A., MARTIN-HERNANDEZ, F., ANDREANI, M., GARRIDO, C.J., SÁNCHEZ-VIZCAÍNO V.L., GÓMEZ-PUGNAIRE M.T., MUÑOZ, M., TRCERA, N. (2015) Redox state of iron during high-pressure serpentinite dehydration. *Contributions to Mineralogy and Petrology* 169, 1–18. <https://doi.org/10.1007/s00410-015-1130-y>
- EVANS, K.A. (2012) The redox budget of subduction zones. *Earth-Science Reviews* 113, 11–32. <https://doi.org/10.1016/j.earscirev.2012.03.003>
- EVANS, K.A., FROST, B.R. (2021) Deserpentinization in subduction zones as a source of oxidation in arcs: A reality check. *Journal of Petrology* 62, 1–32. <https://doi.org/10.1093/petrology/egab016>
- FRANTZ, J.D., POPP, R.K., BOCTOR, N.Z. (1981) Mineral-solution equilibria-V. Solubilities of rock-forming minerals in supercritical fluids. *Geochimica et Cosmochimica Acta* 45, 69–77. [https://doi.org/10.1016/0016-7037\(81\)90264-7](https://doi.org/10.1016/0016-7037(81)90264-7)
- FROST, D.J., MCCAMMON, C.A. (2008) The Redox State of Earth's Mantle. *Annual Review of Earth and Planetary Sciences* 36, 389–420. <https://doi.org/10.1146/annurev.earth.36.031207.124322>
- HERMANN, J., SPANDLER, C.J. (2008) Sediment melts at sub-arc depths: An experimental study. *Journal of Petrology* 49, 717–740. <https://doi.org/10.1093/petrology/egm073>
- HERMANN, J., SPANDLER, C., HACK, A., KORSKOV, A.V. (2006) Aqueous fluids and hydrous melts in high-pressure and ultra-high pressure rocks: Implications for element transfer in subduction zones. *Lithos* 92, 399–417. <https://doi.org/10.1016/j.lithos.2006.03.055>
- KELLEY, K.A., COTTRELL, E. (2009) Water and the oxidation state of subduction zone magmas. *Science* 325, 605–607. <https://doi.org/10.1126/science.1174156>
- LOUVEL, M., SANCHEZ-VALLE, C., MALFAIT, W.J., TESTEMALE, D., HAZEMANN, J.L. (2013) Zr complexation in high pressure fluids and silicate melts and implications for the mobilization of HFSE in subduction zones. *Geochimica et Cosmochimica Acta* 104, 281–299. <https://doi.org/10.1016/j.gca.2012.11.001>
- MANNING, C.E., WILKE, M., SCHMIDT, C., CAUZID, J. (2008) Rutile solubility in albite-H₂O and Na₂Si₃O₇-H₂O at high temperatures and pressures by in-situ synchrotron radiation micro-XRF. *Earth and Planetary Science Letters* 272, 730–737. <https://doi.org/10.1016/j.epsl.2008.06.004>
- MANNING, C.E., ANTIGNANO, A., LIN, H.A. (2010) Premelting polymerization of crustal and mantle fluids, as indicated by the solubility of albite+paragonite+quartz in H₂O at 1 GPa and 350–620°C. *Earth and Planetary Science Letters* 292, 325–336. <https://doi.org/10.1016/j.epsl.2010.01.044>
- MARSCHALL, H.R., SCHUMACHER, J.C. (2012) Arc magmas sourced from mélange diapirs in subduction zones. *Nature Geoscience* 5, 862–867. <https://doi.org/10.1038/ngeo1634>
- MYSEN, B., RICHEL, P. (2019) Chapter 11 - Structure of Iron Silicate Glasses and Melts. In: MYSEN, B., RICHEL, P. (Eds.) *Silicate Glasses and Melts*. Second Edition, Elsevier, Amsterdam, Oxford, Cambridge, 403–430. <https://doi.org/10.1016/B978-0-444-63708-6.00011-9>
- PARKINSON, I.J., ARCULUS, R.J. (1999) The redox state of subduction zones: Insights from arc-peridotites. *Chemical Geology* 160, 409–423. [https://doi.org/10.1016/S0009-2541\(99\)00110-2](https://doi.org/10.1016/S0009-2541(99)00110-2)
- PICCOLI, F., HERMANN, J., PETTKE, T., CONNOLLY, J.A.D., KEMPE, E.D., VIEIRA DUARTE, J.F. (2019) Subducting serpentinites release reduced, not oxidized, aqueous fluids. *Scientific Reports* 9, 1–7. <https://doi.org/10.1038/s41598-019-55944-8>
- SCHOLTEN, L., SCHMIDT, C., LECUMBERRI-SANCHEZ, P., NEWVILLE, M., LANZIROTTI, A., SIRBESCU, M.L.C., STEELE-MACINNIS, M. (2019) Solubility and speciation of iron in hydrothermal fluids. *Geochimica et Cosmochimica Acta* 252, 126–143. <https://doi.org/10.1016/j.gca.2019.03.001>
- SIMON, A.C., PETTKE, T., CANDELA, P.A., PICCOLI, P.M., HEINRICH, C.A. (2004) Magnetite solubility and iron transport in magmatic-hydrothermal environments. *Geochimica et Cosmochimica Acta* 68, 4905–4914. <https://doi.org/10.1016/j.gca.2004.05.033>
- SVERJENSKY, D.A., HARRISON, B., AZZOLINI, D. (2014) Water in the deep Earth: The dielectric constant and the solubilities of quartz and corundum to 60 kb and 1200°C. *Geochimica et Cosmochimica Acta* 129, 125–145. <https://doi.org/10.1016/j.gca.2013.12.019>
- SYRACUSE, E.M., VAN KEKEN, P.E., ABERS, G.A. (2010) The global range of subduction zone thermal models. *Physics of the Earth and Planetary Interiors* 183, 73–90. <https://doi.org/10.1016/j.pepi.2010.02.004>
- TIRABOSCHI, C., MIOZZI, F., TUMIATI, S. (2022) Carbon-saturated COH fluids in the upper mantle: a review of high-pressure and high-temperature ex situ experiments. *European Journal of Mineralogy* 34, 59–75. <https://doi.org/10.5194/ejm-34-59-2022>
- TOLLAN, P., HERMANN, J. (2019) Arc magmas oxidized by water dissociation and hydrogen incorporation in orthopyroxene. *Nature Geoscience* 12, 667–671. <https://doi.org/10.1038/s41561-019-0411-x>
- WALTERS, J.B., CRUZ-URIBE, A.M., MARSCHALL, H.R. (2020) Sulfur loss from subducted altered oceanic crust and implications for mantle oxidation. *Geochemical Perspectives Letters* 13, 36–41. <https://doi.org/10.7185/geochemlet.2011>
- WILKE, M., BEHRENS, H., BURKHARD, D.J.M., ROSSANO, S. (2002) The oxidation state of iron in silicic melt at 500 MPa water pressure. *Chemical Geology* 189, 55–67. [https://doi.org/10.1016/S0009-2541\(02\)00042-6](https://doi.org/10.1016/S0009-2541(02)00042-6)
- WILKE, M., SCHMIDT, C., DUBRAIL, J., APPEL, K., BORCHERT, M., KVASHNINA, K., MANNING, C.E. (2012) Zircon solubility and zirconium complexation in H₂O+Na₂O+SiO₂±Al₂O₃ fluids at high pressure and temperature. *Earth and Planetary Science Letters* 349–350, 15–25. <https://doi.org/10.1016/j.epsl.2012.06.054>
- WYKES, J.L., NEWTON, R.C., MANNING, C.E. (2008) Solubility of andradite, Ca₃Fe₂Si₃O₁₂, in a 10 mol% NaCl solution at 800 °C and 10 kbar: Implications for the metasomatic origin of grandite garnet in calc-silicate granulites. *American Mineralogist* 93, 886–892. <https://doi.org/10.2138/am.2008.2736>



Preferential mobilisation of oxidised iron by slab-derived hydrous silicate melts

C. Tiraboschi, C. McCammon, A. Rohrbach, S. Klemme,
J. Berndt, C. Sanchez-Valle

Supplementary Information

The Supplementary Information includes:

- Materials and Methods
- Calculation of Fe^{3+} Transferred by Hydrous Melts in Subduction Zones
- Tables S-1 to S-3
- Figures S-1 to S-4
- Supplementary Information References

Materials and Methods

Starting materials and piston cylinder experiments

Natural hematite and magnetite, either as a fine-grained powder (1:1 molar ratio) or as single crystals, were employed as starting materials, together with a synthetic haplogranite glass and a source of fluid.

The haplogranite glass employed here, $\text{Na}_{0.56}\text{K}_{0.38}\text{Al}_{0.95}\text{Si}_{5.19}\text{O}_{12.2}$, is silica-rich ($\text{Si}/(\text{Si}+\text{Al}) = 0.86$) and slightly peralkaline ($(\text{Na} + \text{K})/\text{Al} = 1.13$; $\text{Na}/\text{K} = 0.9$) as shown in Table S-1 (Ardia *et al.*, 2008, 2014).

Experiments were conducted in an end-loaded piston cylinder apparatus at WWU Münster with two different fluid systems: i) H_2O -only or ii) H_2O -NaCl solution with a concentration of 1.5 m NaCl (~8 wt. % NaCl, ~4.9 wt. % Cl) to approximate the salinity of island-arc setting slab-derived fluids (*e.g.*, Kent *et al.*, 2002). Variable amounts of fluid were added to the experimental charges (Table S-1) to guarantee hydrous conditions of the coexisting melt at run conditions, *i.e.* below the critical curve for the haplogranite- H_2O system (Bureau and Keppler, 1999; Fig. 1). Run duration varied from 24 hours for high-temperature experiments (*i.e.* 900 °C) to 72 hours in low-temperature runs (*i.e.* 700 °C) to ensure equilibration (see discussion below).



The oxygen fugacity conditions were constrained by the simultaneous presence of magnetite and hematite (HM buffer), which is between -11.3 (2 GPa, 700 °C, ΔFMQ 3.8) and -6.4 (1 GPa, 950 °C, ΔFMQ 4.8) expressed as $\log f\text{O}_2$ (Table 1). Fixing the oxygen fugacity conditions brings some important constraints to our experimental strategy, as at buffered conditions the only iron exchange in the experimental capsule would derive from the dissolution process, and not from redox reactions occurring between hematite and magnetite. Moreover, the imposed redox conditions are comprised into the range of oxygen fugacities expected in subduction mélanges (see Cannà and Malaspina, 2018 and ref. therein).

Oxygen fugacities at the experimental conditions are expressed as $\log f\text{O}_2$ and were calculated employing the software package *Perple_X* (Connolly, 1995) and the thermodynamic dataset of Holland and Powell (1998). In the experimental runs in which only magnetite or hematite are present the oxygen fugacity is unconstrained.

Starting materials (*i.e.* hematite, magnetite, glass, and fluid) were loaded in gold capsules (3 mm outer diameter, ~ 7 mm length), mounted on steel support stored at -20 °C, and welded shut, to avoid fluid loss during welding. Capsules were loaded in a MgO–Pyrex–talc assembly. The temperature was measured through W_{97}Re_3 – $\text{W}_{75}\text{Re}_{25}$ thermocouples and is considered accurate within ± 10 °C. Pressure calibration of the apparatus is based on the quartz-coesite transition (Bose and Ganguly, 1995) and the $\text{MgCr}_2\text{O}_4 + \text{SiO}_2 = \text{MgSiO}_3 + \text{Cr}_2\text{O}_3$ reaction (Klemme and O'Neill, 1997), and a friction correction of -13% was applied to the nominal pressure. Pressures are considered accurate to 0.01 GPa. In all runs, fragments of the original hematite and/or magnetite were recovered from the capsule after quench, demonstrating saturation during the experiment. Experiments performed at buffered conditions showed no formation of new crystals of magnetite or hematite. All runs showed excess fluid upon capsule puncturing and the presence of water in the recovered glass fragment was confirmed by Raman spectroscopy.

Attainment of equilibrium in the experimental runs

Attainment of equilibrium conditions was confirmed by time series experiments performed at the same pressure, temperature, and oxygen fugacity conditions, with run durations ranging from 24 to 72 hours. For instance, experiments performed within 24 hours (GHM1) and 72 hours (GHM5) at 1 GPa and 800 °C display similar values of FeO in the quenched glass within error (Table S-1), showing no major difference even for shorter experimental runs. Moreover, experiments performed at similar P , T , and $f\text{O}_2$ conditions employing either powders or single-crystals of hematite and magnetite yield comparable FeO values (*e.g.*, GHM5 and GHM2, Table S-1), demonstrating little effect of the grain size on FeO content as well as equilibration during the experiments.

Achievement of redox equilibrium in our experiments is expected due to the long run duration, *i.e.* above 24 hours, which is significantly longer than the redox equilibration times of 3–10 hours reported for hydrous metaluminous or peralkaline melts with approximately 1–3 wt. % of total FeO at 800 °C and 0.2 GPa by Gaillard *et al.* (2002). Moreover, the redox ratio of iron and the hyperfine parameters of ferric and ferrous iron determined by Mössbauer spectroscopy in the recovered glasses should not be affected by fast quenching rates (Mysen, 2006).

Analytical techniques

Major element concentrations of quenched glasses, hematite, and magnetite were determined with a 5-spectrometer JEOL JXA 8530F electron microprobe (EMP) at the Institute of Mineralogy, WWU Münster. Analyses of the quenched glasses were performed with an accelerating voltage of 15 keV and a beam current of 10 nA, with variable beam sizes ranging from 5 to 20 μm on homogenous parts of the glass, *i.e.* free from Fe oxides grains and vapour bubbles (Fig. S-1a,b). The homogeneity of the glasses was checked by repeated analyses in different areas of the sample and by optical examination to confirm the absence of microscopic mineral phases. The signal from Na was monitored during the measurements and no significant loss was observed. Samples major elements analyses are summarised in Table S-1.

Mössbauer absorption spectra were collected at Bayerisches Geoinstitut (BGI), University of Bayreuth on samples GHM9, GHM10, GH2, and GM1, which present high FeO content. Glass pieces were mounted on plastic film using clear nail varnish to form a mosaic of approximately 2 mm diameter and 1 mm thick. This corresponds to a Mössbauer thickness of roughly 4 mg Fe/cm², which is close to the optimum for these compositions. Spectra were collected in



transmission mode on a constant acceleration Mössbauer spectrometer with a nominal 370 MBq ^{57}Co point source in a 12 μm Rh matrix with active dimension of $500 \times 500 \mu\text{m}^2$. The velocity scale was calibrated with Fe foil. Spectra were collected at room temperature over a velocity scale of $\pm 5 \text{ mm/s}$ with measuring times of approximately 7 days each. Spectra were fitted using MossA software (Prescher *et al.*, 2012).

Thermodynamic modelling

We employed the DEW model (Sverjensky *et al.*, 2014; Huang and Sverjensky, 2019; Sverjensky, 2019) coupled with the Fortran code EQ3NR (Wolery, 1992) to calculate the solubility of hematite and magnetite in H_2O , H_2O -NaCl fluids and fluids equilibrated with a dissolved silica species. The DEW model employs the Helgeson-Kirkham-Flowers (HKF) equations of state for aqueous species (Helgeson *et al.*, 1981; Shock and Helgeson, 1988, 1990; Tanger and Helgeson, 1988; Shock *et al.*, 1989, 1997) together with revised predictive correlations between the equation of state coefficients and the standard partial molal properties of aqueous species (Facq *et al.*, 2014; Sverjensky *et al.*, 2014; Sverjensky, 2019) to calculate the apparent standard partial molal Gibbs free energies of aqueous species at high pressures and temperatures. Equilibrium constants are then incorporated in the Fortran code EQ3NR (Wolery, 1992) to compute aqueous speciation and solubility models, providing total dissolved concentrations of each element and the saturation state of the associated fluid with respect to the minerals in the system.

The first set of solubilities was calculated from 700 to 1000 $^\circ\text{C}$ and from 1 to 2 GPa considering the H_2O -only and the H_2O -NaCl systems. The input file was constructed in order to have hematite and magnetite coexisting at fixed oxygen fugacity conditions. The second set of calculations was performed by adding appropriate amounts of $\text{Si}(\text{OH})_4$, to account for the presence of a silicate melt and to evaluate the possible influence of dissolved silica on iron transport. Results from modelling are reported in Table S-3.

Since to our knowledge, no experimental data are available for the solubility of haplogranite melts in H_2O and H_2O -NaCl fluids, the composition of the aqueous fluid was estimated from experimental data (see Louvel *et al.*, 2020) on albite dissolution in H_2O (Manning *et al.*, 2010; Wohlers *et al.*, 2011). Silica contents in the fluid were exponentially extrapolated to higher temperatures (*i.e.* 900 $^\circ\text{C}$) following Manning *et al.* (2010), which showed a strong increase in the solute content at near-solidus conditions in the system albite + paragonite + quartz + H_2O , possibly due to the presence of more polymerized species (Newton and Manning, 2008).

Mössbauer absorption results

The Mössbauer spectra recorded on the four investigated samples are shown in Figure S-2 and the results are presented below. The Mössbauer spectra fitting parameters, including the centre shift (CS) and quadrupole splitting (QS) (Fig. S-3), as well as the calculated $\text{Fe}^{3+}/\text{Fe}_{\text{tot}}$ ratios are summarised in Table S-2.

GHM9

The spectrum (Fig. S-2a) can be fit to two doublets with Voigt lineshape (Gaussian distribution of Lorentzians). The green doublet is assigned to Fe^{3+} and the blue doublet to Fe^{2+} . The blue doublet has a centre shift of 1.16, which is higher than expected for a glass. This can be attributed to its presence as precipitates from the fluid phase. The bulk value of $\text{Fe}^{3+}/\text{Fe}_{\text{tot}}$ can be calculated from the relative areas as 0.79 ± 0.04 .

GHM10

The spectrum can be fit to two doublets as sample GHM9, with the addition of a sextet (Fig. S-2b). Only the inner four lines of the sextet are observed due to small velocity scale, but all positions are consistent with hematite. The two doublets have the same hyperfine parameters (centre shift and quadrupole splitting) as those in sample GHM9 (Table S-2), indicating that Fe^{2+} is mainly present as precipitates from the fluid phase. The bulk value of $\text{Fe}^{3+}/\text{Fe}_{\text{tot}}$ considering the doublets only and excluding the hematite from the calculation is 0.45 ± 0.07 .



GH2

The prominent doublet (dark green) has parameters consistent with tetrahedral Fe³⁺ (Fig. S-2c). A broad doublet (blue) is consistent with Fe³⁺ but with higher coordination. A broad doublet with higher centre shift and quadrupole splitting (medium green) is assigned to Fe²⁺, also in this case attributed to the presence of precipitates. Magnetic peaks could be fit to the data and parameters correspond to hematite. The calculated Fe³⁺/Fe_{tot} is retrieved from relative areas excluding the contribution of hematite and corresponds to 0.73±0.22.

GMI

Doublets assigned to glass components are similar to those in the previous spectrum except that the Fe²⁺ doublet is noticeably more intense compared to GH2 (Fig. S-2d). There is a broad absorption (blue) that could arise from a weak magnetic interaction, for example very small particles of ferric iron oxide (around a few tens of nanometres grain size). The Fe³⁺/Fe_{tot} is calculated from relative areas, excluding the contribution of the small particles of iron oxides, and corresponds to 0.64±0.15.

Overall, the data show that Fe³⁺ is mainly present in the melt structure, probably in more than one coordination environment. Parameters reported in Table S-2 are consistent with Fe³⁺ in tetrahedral coordination and possibly higher values (IV or VI, or a mixture of both). On the other hand, Fe²⁺ seems to be present for the most part as precipitates from the aqueous fluid, as shown by high values of centre shift (CS) and quadrupole splitting (QS) (Fig. S-3). However, due to the Fe²⁺ broad absorption, it is not possible to exclude the presence of Fe²⁺ also in the melt structure.

Unbuffered experimental runs

The two unbuffered experiments (Fig. S-1c,d) resulted in slightly lower Fe³⁺/FeO_{tot} ratios: 0.73±0.22 for the quenched glass in equilibrium with hematite and 0.64±0.15 for the glass in equilibrium with magnetite at 1 GPa and 900 °C in the H₂O + melt system. The difference is mainly ascribable to the Fe²⁺ content, as the calculated amount of Fe³⁺ in the glass is similar for both experiments (*i.e.* 1.10 wt. % for magnetite + hydrous melt, and 1.15 wt. % for hematite + hydrous melt experiment, see Table S-1). However, due to the low amount of total iron in the system, which leads to a significant error in the retrieved Fe³⁺/Fe_{tot} ratio obtained by Mössbauer spectroscopy, it is difficult to assess if the two unbuffered experiments equilibrated at the same Fe³⁺/Fe²⁺ ratio.

These results highlight the importance to investigate the dissolution process at buffered conditions, to avoid redox reactions between hematite and magnetite, which could influence the amount of iron mobilised in the system. For instance, in the hematite-only experiment, Mössbauer absorption spectra indicate the presence of Fe²⁺, which likely derives from a redox reaction. Moreover, some redox reactions probably also occur in the magnetite-only experiment, which showed some reaction rims suggesting the formation of hematite (Fig. S-1d).

Calculation of Fe³⁺ Transferred by Hydrous Melts in Subduction Zones

The experimental results presented were further employed to provide constraints on the amount of Fe³⁺ transferred by hydrous melts from hematite and magnetite, which is crucial information to evaluate the redox budget of subduction zones (Evans, 2006, 2012; Evans and Tomkins, 2011).

Here we considered the Fe³⁺ content at 2 GPa and 900 °C (sample GHM9 and GHM10) in both systems: H₂O + melt and H₂O-NaCl + melt to constrain the Fe³⁺ fluxes associated with hematite–magnetite dissolution in hydrous melts at subduction zone conditions.

The Fe₂O₃ content in the quenched glass was calculated from the Fe³⁺/Fe_{tot} ratio derived from the Mössbauer absorption spectra and from the total FeO content obtained by electron microprobe analyses (Table 1 and Table S-1). In the H₂O + melt system, the Fe₂O₃ corresponds to 1.59 wt. % while in the H₂O-NaCl + melt system equals 0.98 wt. % (Fig. S-4).



Because the iron redox ratios in silicate melts are linearly proportional to the oxygen fugacity conditions on a logarithmic scale (Kress and Carmichael, 1991; Wilke *et al.*, 2002; Botcharnikov *et al.*, 2005) we can extrapolate the possible Fe³⁺ content in hydrous melt in equilibrium with magnetite and hematite to lower temperature conditions, in order to approximate conditions compatible with hot subduction geotherms paths (*e.g.*, Syracuse *et al.* 2010) as shown in Fig. 1.

We considered two possible correlations between the Fe³⁺/Fe²⁺ ratio and the oxygen fugacity. The first one is derived from the empirical equation of Kress and Carmichael (1991) and it has been calculated from experimental data at 2 GPa and 900 °C. The second curve slope considered is derived from experimental Mössbauer absorption data of hydrous silicate melts from Wilke *et al.* (2002), obtained at 0.5 GPa and temperatures of 850 and 950 °C. The two different linear correlations define two areas, which represent the possible Fe³⁺/Fe²⁺ ratios depending on the oxygen fugacity conditions. Since the simultaneous presence of hematite and magnetite in the system define the *f*O₂ at fixed pressure and temperature, it is possible to calculate the possible Fe₂O₃ content of hydrous melts in equilibrium with hematite and magnetite to lower temperature conditions, more compatible with a hot subducting slab geotherm (see Fig. 1).

In the H₂O + melt system the expected Fe³⁺ content calculated ranges from 0.15 to 0.23 wt. %, up to the measured values of 1.59 wt. % at 2 GPa and 900 °C (*f*O₂ = -6.9, ΔFMQ 4.0). In the H₂O-NaCl + melt system the retrieved Fe³⁺ ranges from 0.05 to 0.08 wt. % at 2 GPa and 700 °C (*f*O₂ = -11.5, ΔFMQ 3.8), reaching values of 0.98 wt. % at 2 GPa and 900 °C (*f*O₂ = -6.9, ΔFMQ 4.0). These values provide the amount of oxidised iron mobilised from hematite and magnetite dissolution by hydrous silicate melts at conditions compatible with a hot subduction slab.

Comparison with previous studies

The FeO concentrations in hydrous haplogranite glasses retrieved here compare well with the results from experimental studies of sediment melting at sub-arc conditions (Hermann *et al.*, 2006; Hermann and Spandler, 2008). These experiments, conducted at slightly higher pressures, *i.e.* 2.5 GPa, report FeO contents in the quenched hydrous glass ranging from 1.04 wt. % (16 wt. % H₂O) at 750 °C to 1.26 wt. % at 800 °C (10 wt. % H₂O). For comparison, we report a FeO content of 0.96 wt. % at 2 GPa, 800 °C in the H₂O-only system (9.39 wt. % H₂O).

Moreover, our results are also consistent with FeO contents determined in natural melt inclusions from mantle xenoliths. Although mantle xenoliths from the subarc upper mantle are quite rare, few examples can be considered for comparison. For instance, hornblende peridotite xenoliths from central Mexico (Blatter and Carmichael, 1998) show oxygen fugacity comprises between ΔFMQ 1.5 and 2.4, locally up to 4 in presence of hematite and magnetite. The FeO content in the silicate glass, *i.e.* 1.02 wt. %, is compatible with our results at similar pressure and temperature conditions (*i.e.* 1.5 GPa and 800 °C). Similar FeO content, 1.27 wt. %, and 8.1 wt. % H₂O, has been also measured in melt inclusions from mantle xenoliths from the Avacha volcano in Kamchatka (Ionov *et al.*, 2011).

Geological environments

The investigated experimental system represents a simplified subduction slab setting, in which Fe-oxides interact with a haplogranitic composition. The Fe-source is exclusively represented by magnetite and hematite, which are common in subduction zone settings, for instance in serpentinites (*e.g.*, Carbonin *et al.*, 2015; Debret *et al.*, 2015) and in metasediments (*e.g.*, Tumiati *et al.*, 2015; Ague *et al.*, 2022). Our results thus have direct implications for two possible geological environments where interactions between hydrous (haplo)granitic melts with magnetite–hematite occurs. First, the melt is produced by magnetite and hematite-bearing metasediments. Metasediments constitute a layer thick up to 400 m (Van Keken *et al.*, 2011) above the altered oceanic crust, and often contain oxidised Fe³⁺-bearing sedimentary detritus (Ague *et al.*, 2022 and ref. therein). Highly oxidised metasediments from exhumed subduction complexes have been observed in the Alps (Tumiati *et al.*, 2015) and in other locations (see Cannà and Malaspina, 2018). Recently Ague *et al.* (2022) showed that highly oxidised metasedimentary rocks, containing hematite and magnetite, have the capacity of oxidising the fluid released from the slab. The granitic melt generated at these conditions would be in equilibrium with magnetite and hematite, consequently, it will efficiently dissolve Fe from these phases, and would transfer the oxidised signature directly to the mantle wedge. Second, the hydrous silicate melt is generated by metasediment slices present in the subduction mélange (Marschall and Schumacher, 2012; Nielsen and Marschall, 2017),



and interacts with serpentinite slices. Similarly to the first environment, the resulting melt will then reach the mantle wedge and efficiently transfer Fe^{3+} to the source of arc magmas.



Supplementary Tables

Table S-1 Major element compositions (in wt. %) of the starting haplogranitic composition (HGG) and quenched glasses determined by electron microprobe. Uncertainties are reported below the average values for each glass as 1 standard deviation of n ($10 < n < 50$) analyses performed on the glass. H₂O concentrations were not analysed; the reported values are obtained by subtracting the total of major element analyses from 100. FeO* and Fe₂O₃* refer to the calculated amounts of Fe²⁺ and Fe³⁺ considering the Fe³⁺/Fe_{tot} ratios obtained by Mössbauer spectroscopy.

	<i>P</i> (GPa)	<i>T</i> (°C)	run time (h)	starting fluid	fluid (wt. %)	Na ₂ O	MgO	Al ₂ O ₃	SiO ₂	K ₂ O	CaO	Cl	FeO	TiO ₂	Cr ₂ O ₃	MnO	Total	H ₂ O	FeO*	Fe ₂ O ₃ *
HGG						4.52	0.00	11.73	78.53	4.47	0.01	0.01	0.02	0.03	0.01	0.01	99.37			
						0.10	0.01	0.06	0.16	0.11	0.01	0.01	0.01	0.03	0.01	0.01	0.21			
GHM3	1	700	48	H ₂ O	19.37	3.34	0.01	10.72	71.29	3.85	0.03	0.00	0.60	0.02	0.01	0.01	89.88	10.12		
						0.17	0.01	0.14	0.69	0.09	0.02	0.00	0.21	0.03	0.01	0.02	0.85			
GHM6	1	700	48	1.5 m H ₂ O-NaCl	27.39	3.73	0.00	11.46	68.76	4.28	0.02	0.05	0.75	0.02	0.02	0.01	89.11	10.89		
						0.32	0.01	0.15	0.64	0.27	0.02	0.01	0.08	0.03	0.02	0.02	0.34			
GHM1	1	800	24	H ₂ O	41.94	2.94	0.01	10.82	71.34	3.92	0.04	0.01	1.04	0.02	0.01	0.03	90.17	9.83		
						0.32	0.01	0.15	0.96	0.11	0.02	0.01	0.12	0.02	0.02	0.03	0.70			
GHM7	1	800	24	1.5 m H ₂ O-NaCl	21.43	2.59	0.02	10.74	72.17	4.52	0.04	0.11	1.50	0.01	0.01	0.04	91.70	8.30		
						0.48	0.02	0.14	1.02	0.56	0.02	0.02	0.31	0.01	0.02	0.02	1.41			
GHM5	1	800	72	H ₂ O	18.10	3.37	0.05	10.54	71.59	3.95	0.02	0.00	1.22	0.03	0.01	0.03	90.82	9.18		
						0.13	0.02	0.16	0.49	0.09	0.01	0.00	0.24	0.02	0.01	0.02	0.67			
GHM2*	1	800	72	H ₂ O	17.83	0.82	0.04	11.18	72.96	3.47	0.11	0.01	1.23	0.01	0.01	0.03	89.87	10.13		
						0.33	0.01	0.22	0.88	0.78	0.03	0.01	0.06	0.02	0.01	0.02	1.25			
GHM4	1	900	24	H ₂ O	23.86	3.13	0.02	10.53	70.38	3.89	0.04	0.00	1.82	0.03	0.01	0.04	89.90	10.10		
						0.21	0.02	0.10	0.49	0.09	0.02	0.00	0.11	0.03	0.01	0.02	0.66			
GHM11	1	900	24	1.5 m H ₂ O-NaCl	27.65	2.70	0.01	10.70	72.70	3.70	0.03	0.15	2.17	0.02	0.01	0.04	92.23	7.77		
						0.30	0.01	0.14	0.81	0.31	0.02	0.08	0.26	0.03	0.01	0.02	1.11			
GM1*	1	900	24	H ₂ O	31.97	2.89	0.03	10.21	71.04	3.79	0.02	0.00	1.61	0.01	0.01	0.03	89.68	10.32	0.62	1.10
						0.26	0.01	0.13	0.56	0.13	0.01	0.01	0.09	0.02	0.01	0.02	0.57			
GH2*	1	900	24	H ₂ O	47.06	2.50	0.02	10.81	72.96	3.66	0.01	0.01	1.42	0.02	0.01	0.01	91.44	8.56	0.38	1.15



GHM13*	1	950	24	H ₂ O	18.69	0.39	0.01	0.11	0.70	0.24	0.01	0.01	0.13	0.02	0.01	0.01	0.70			
						2.99	0.01	10.10	70.95	3.76	0.05	0.01	1.96	0.02	0.01	0.09	89.99	10.01		
						0.24	0.01	0.17	0.96	0.12	0.02	0.01	0.04	0.02	0.01	0.02	1.12			
GHM15*	1	950	24	1.5 m H ₂ O-NaCl	30.77	2.83	0.01	9.99	70.77	3.53	0.03	0.17	2.40	0.02	0.01	0.05	89.87	10.13		
						0.87	0.01	0.22	1.03	0.54	0.02	0.07	0.12	0.02	0.01	0.02	0.67			
GHM19	2	700	48	1.5 m H ₂ O-NaCl	27.81	3.96	0.01	13.53	70.15	3.92	0.00	0.21	0.60	0.02	0.02	0.02	92.46	7.54		
						0.34	0.01	0.18	0.45	0.19	0.01	0.05	0.09	0.03	0.02	0.01	0.53			
GHM20*	2	800	24	H ₂ O	21.76	2.02	0.02	10.64	74.03	2.64	0.02	0.02	0.96	0.02	0.01	0.05	90.61	9.39		
						0.31	0.01	0.20	1.69	0.32	0.02	0.02	0.11	0.03	0.01	0.02	1.74			
GHM9*	2	900	24	H ₂ O	23.56	2.87	0.02	10.61	73.32	3.90	0.02	0.01	1.85	0.02	0.01	0.04	92.66	7.34	0.42	1.59
						0.52	0.01	0.27	0.99	0.19	0.01	0.01	0.18	0.03	0.01	0.02	1.00			
GHM10*	2	900	24	1.5 m H ₂ O-NaCl	29.29	2.25	0.09	10.56	72.12	3.78	0.04	0.18	2.07	0.01	0.01	0.04	91.14	8.86	1.19	0.98
						0.43	0.05	0.49	2.41	0.20	0.02	0.09	0.41	0.02	0.02	0.01	2.66			



Table S-2 Hyperfine parameter values derived from fits of Mössbauer absorption spectra. CS: centre shift; FWHM: full width at half maximum; Int: relative area; QS: quadrupole splitting; BHF: hyperfine magnetic splitting.

		CS (mm/s)	Error (mm/s)	FWHM (mm/s)	Error (mm/s)	Int	Error	QS (mm/s)	Error (mm/s)	BHF (T)	Error (T)	Fe ³⁺ /Fe _{tot}
GHM9	Fe ³⁺	0.33	0.02	0.64	0.09	0.79	0.04	0.94	0.04	-	-	0.79±0.04
	Fe ²⁺	1.16	0.03	0.34	0.08	0.21	0.04	2.46	0.06	-	-	
GHM10	Fe ³⁺	0.31	0.11	0.65	-	0.31	0.07	0.84	0.23	-	-	0.45±0.07
	Fe ³⁺ in hematite	0.33	0.04	0.21	0.19	0.31	0.11	-0.21	-	50.58	0.48	
	Fe ²⁺	1.14	0.05	0.37	0.19	0.38	0.08	2.50	0.11	-	-	
GH2	^{IV} Fe ³⁺	0.33	0.04	0.19	0.12	0.10	0.10	-0.21	-	50.4	0.5	0.73±0.22
	^{VI} Fe ³⁺	0.13	0.02	0.30	0.11	0.24	0.25	0.57	0.04	-	-	
	Fe ³⁺ in hematite	0.33	0.17	0.92	0.46	0.42	0.27	0.86	0.33	-	-	
	Fe ²⁺	1.14	0.29	0.92	0.47	0.24	0.22	2.48	0.59	-	-	
GM1	Fe ³⁺	0.3	0.4	3.3	8.8	0.59	0.31	0	-	4	57	0.64±0.15
	^{IV} Fe ³⁺	0.11	0.02	0.35	0.07	0.18	0.18	0.56	0.05	-	-	
	^{VI} Fe ³⁺	0.38	0.16	0.49	0.37	0.08	0.24	0.72	0.20	-	-	
	Fe ²⁺	1.07	0.16	0.79	0.18	0.14	0.15	2.45	0.40	-	-	



Table S-3 Solubility of hematite and magnetite in H₂O and H₂O-NaCl fluids at 1–2 GPa and from 700 to 1000 °C calculated with the DEW model. Solubility values are given as mol/kg of Fe. Si(OH)₄ contents are also given as mol/kg.

Hematite and magnetite solubility in H ₂ O and H ₂ O-NaCl							
T (°C)	H ₂ O	1 GPa	2 GPa	H ₂ O-NaCl	1 GPa	2 GPa	
700		5.48E-07	1.10E-05		0.004	0.010	
800		2.97E-07	5.30E-06		0.008	0.018	
900		1.77E-07	2.81E-06		0.016	0.032	
1000		1.21E-07	1.70E-06		0.028	0.053	
Hematite and magnetite solubility in H ₂ O and H ₂ O-NaCl + dissolved silica							
T (°C)	H ₂ O	1 GPa	2 GPa	H ₂ O-NaCl	1 GPa	2 GPa	Si(OH) ₄ added
700		0.013	0.043		0.035	0.076	1.5
800		0.014	0.050		0.044	0.095	2.4
900		0.014	0.057		0.054	0.118	5.0
1000		0.014	0.064		0.067	0.149	13.0



Supplementary Figures

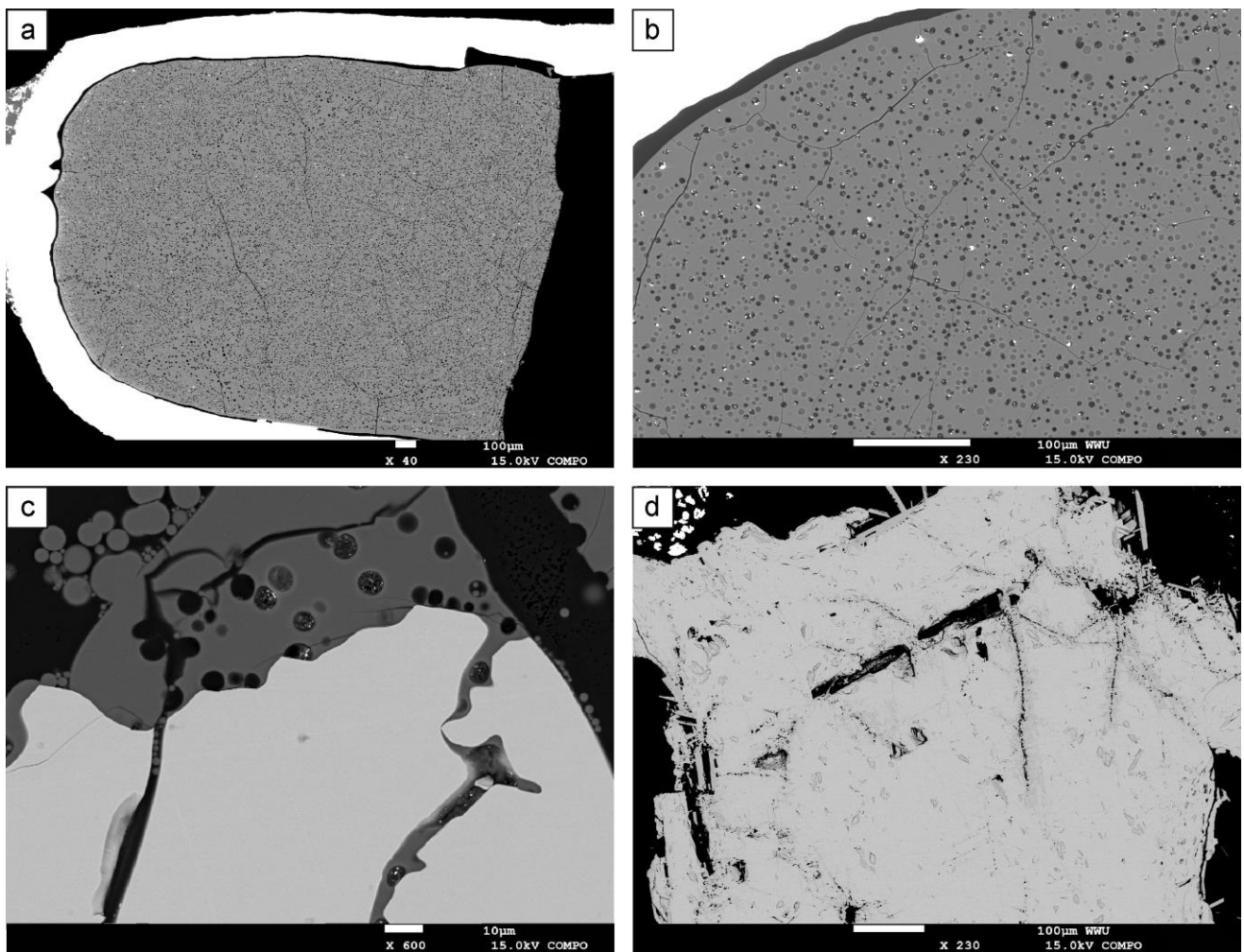


Figure S-1 Backscattered electron images of representative run products: **(a)** quenched hydrous silicate melt ($P = 1$ GPa; $T = 950$ °C, sample GHM13); **(b)** magnified detail of quenched hydrous silicate melt shown in Fig. S-1a. The bright spots are Fe-bearing precipitates, localised in vapor bubbles; **(c)** dissolution feature on a hematite crystal ($P = 1$ GPa, $T = 900$ °C, sample GH2); **(d)** dissolution features on a magnetite crystal ($P = 1$ GPa, $T = 900$ °C, sample GM1).

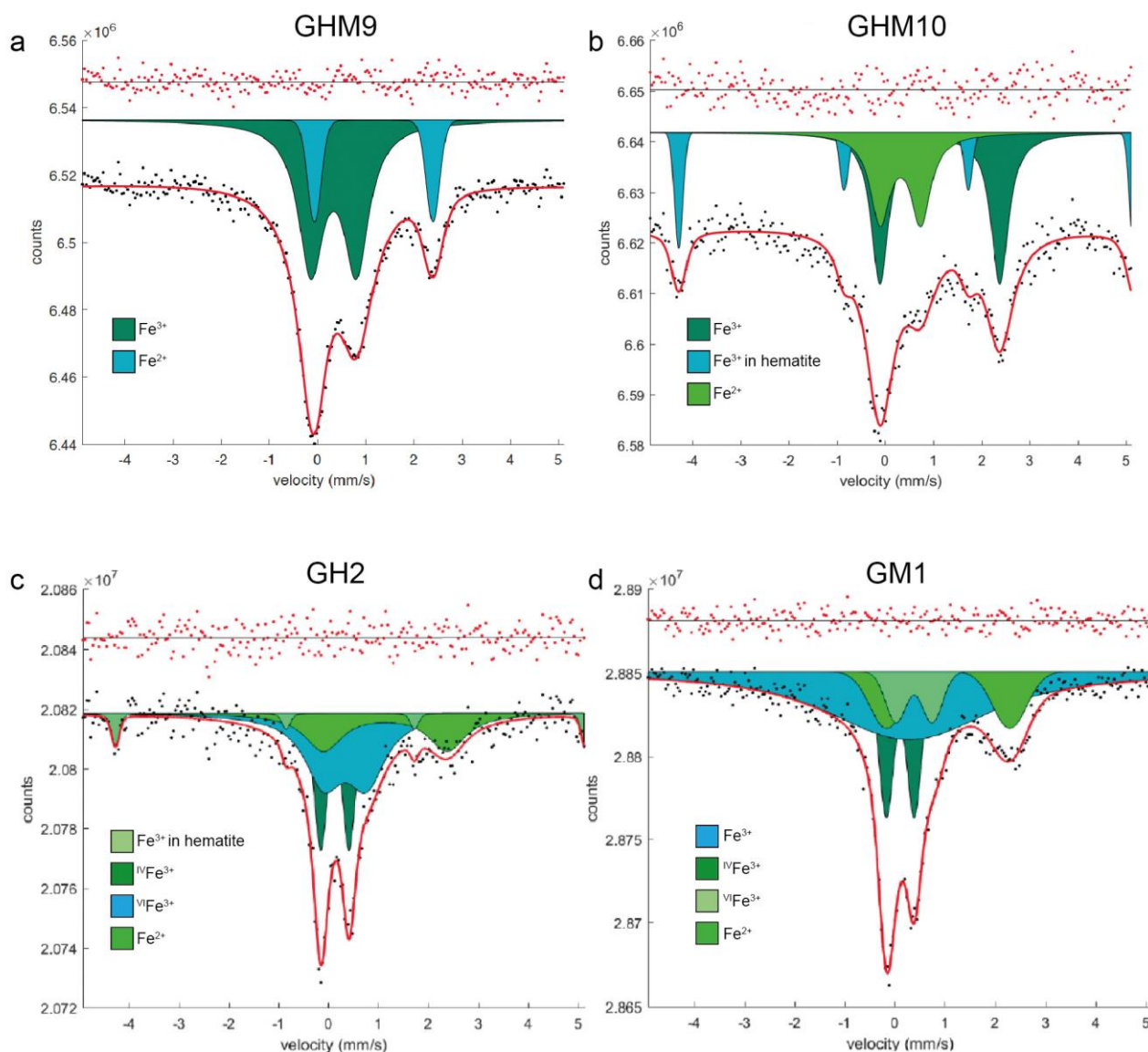


Figure S-2 Mössbauer absorption spectra (a) sample GHM9 ($P = 2$ GPa, $T = 900$ °C) (b) sample GHM10 ($P = 2$ GPa, $T = 900$ °C) (c) sample GH2 ($P = 1$ GPa, $T = 900$ °C) (d) sample GM1 ($P = 1$ GPa, $T = 900$ °C).

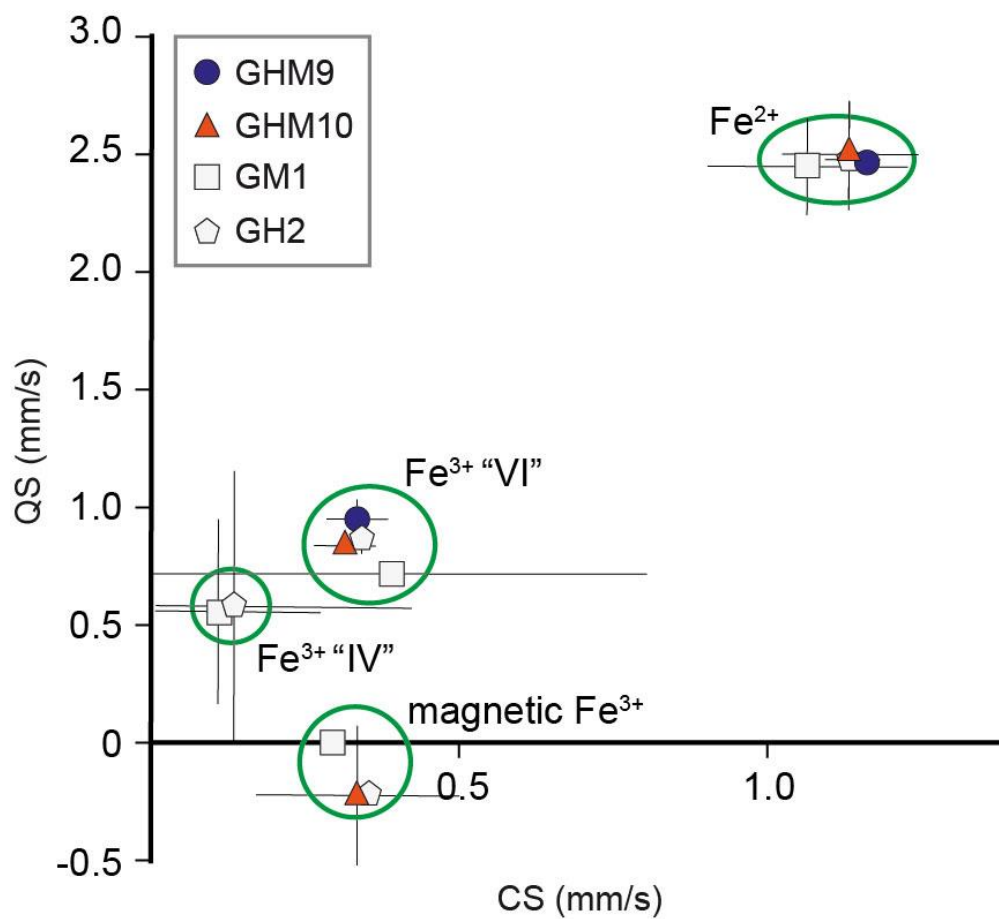


Figure S-3 Centre shift versus quadrupole splitting values derived from fits of the Mössbauer data.

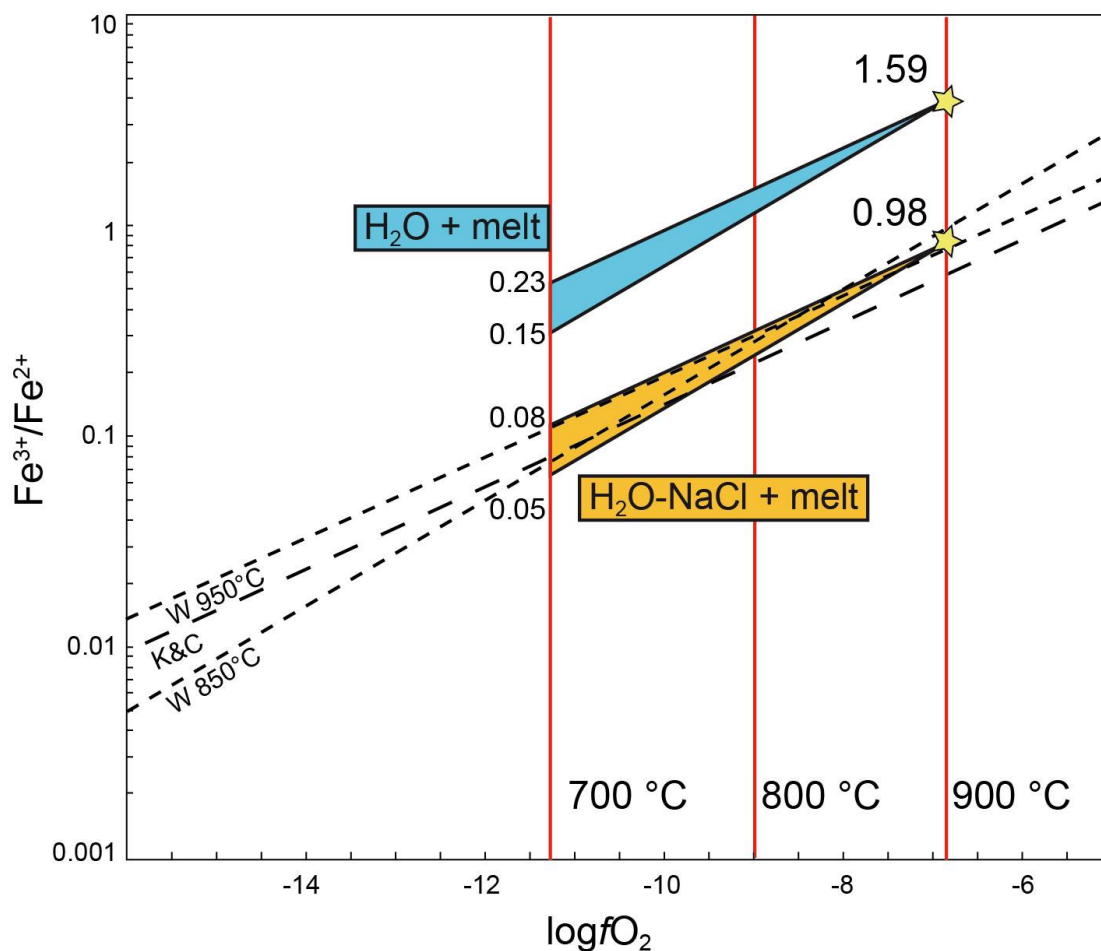


Figure S-4 Oxygen fugacity (reported as $\log f_{\text{O}_2}$) plotted versus $\text{Fe}^{3+}/\text{Fe}^{2+}$ ratios. $\text{Fe}^{3+}/\text{Fe}^{2+}$ ratios determined from Mössbauer spectra at 2 GPa and 900 °C are denoted by the stars. Long dashed line: redox ratios after Kress and Carmichael (1991) calculated at 2 GPa and 900 °C. Short-dashed lines: redox ratio from Wilke *et al.* (2002) at 0.5 GPa. The coloured areas correspond to the predicted $\text{Fe}^{3+}/\text{Fe}^{2+}$ ratio in the $\text{H}_2\text{O} + \text{melt}$ and the $\text{H}_2\text{O-NaCl} + \text{melt}$ system extrapolated from experimental data at 2 GPa and 900 °C to lower temperature conditions. The reported numbers correspond to the amount of Fe_2O_3 , expressed in wt. %.

Supplementary Information References

- Ague, J.J., Tassara, S., Holycross, M.E., Li, J.-L., Cottrell, E., Schwarzenbach, E.M., Fassoulas, C., John, T. (2022) Slab-derived devolatilization fluids oxidized by subducted metasedimentary rocks. *Nature Geoscience* 15, 320–326. <https://doi.org/10.1038/s41561-022-00904-7>
- Ardia, P., Giordano, D., Schmidt, M.W. (2008) A model for the viscosity of rhyolite as a function of H₂O-content and pressure: A calibration based on centrifuge piston cylinder experiments. *Geochimica et Cosmochimica Acta* 72, 6103–6123. <https://doi.org/10.1016/j.gca.2008.08.025>
- Ardia, P., Di Muro, A., Giordano, D., Massare, D., Sanchez-Valle, C., Schmidt, M.W. (2014) Densification mechanisms of haplogranite glasses as a function of water content and pressure based on density and Raman data. *Geochimica et Cosmochimica Acta* 138, 158–180. <https://doi.org/10.1016/j.gca.2014.03.022>
- Blatter, D.L., Carmichael, I.S.E. (1998) Hornblende peridotite xenoliths from central Mexico reveal the highly oxidized nature of subarc upper mantle. *Geology* 26, 1035–1038. [https://doi.org/10.1130/0091-7613\(1998\)026%3C1035:HPXFCM%3E2.3.CO;2](https://doi.org/10.1130/0091-7613(1998)026%3C1035:HPXFCM%3E2.3.CO;2)
- Bose, K., Ganguly, J. (1995) Quartz-coesite transition revisited: reversed experimental determination at 500–1200°C and retrieved thermochemical properties. *American Mineralogist* 80, 231–238. <https://doi.org/10.2138/am-1995-3-404>
- Botcharnikov, R.E., Koepke, J., Holtz, F., McCammon, C., Wilke, M. (2005) The effect of water activity on the oxidation and structural state of Fe in a ferro-basaltic melt. *Geochimica et Cosmochimica Acta* 69, 5071–5085. <https://doi.org/10.1016/j.gca.2005.04.023>
- Bureau, H., Keppler, H. (1999) Complete miscibility between silicate melts and hydrous fluids in the upper mantle: Experimental evidence and geochemical implications. *Earth and Planetary Science Letters* 165, 187–196. [https://doi.org/10.1016/S0012-821X\(98\)00266-0](https://doi.org/10.1016/S0012-821X(98)00266-0)
- Cannaò, E., Malaspina, N. (2018) Geosphere From oceanic to continental subduction : implications for the geochemical and redox evolution of the supra-subduction mantle. *Geosphere* 14, 2311–2336. <https://doi.org/10.1130/GES01597.1>
- Carbonin, S., Martin, S., Tumiatei, S., Rossetti, P. (2015) Magnetite from the Cogne serpentinites (Piemonte ophiolite nappe, Italy). Insights into seafloor fluid–rock interaction. *European Journal of Mineralogy* 27, 31–50. <https://doi.org/10.1127/ejm/2014/0026-2410>
- Connolly, J.A.D. (1995) Phase diagram methods for graphitic rocks and application to the system C–O–H–FeO–TiO₂–SiO₂. *Contributions to Mineralogy and Petrology* 119, 94–116. <https://doi.org/10.1007/BF00310720>
- Debret, B., Bolfan-Casanova, N., Padron-Navarta, J.A., Martin-Hernandez, F., Andreani, M., Garrido, C.J., Sánchez-Vizcaíno V.L., Gómez-Pugnaire M.T., Muñoz, M., Trcera, N. (2015) Redox state of iron during high-pressure serpentinite dehydration. *Contributions to Mineralogy and Petrology* 169, 1–18. <https://doi.org/10.1007/s00410-015-1130-y>
- Evans, K.A. (2006) Redox decoupling and redox budgets: Conceptual tools for the study of earth systems. *Geology* 34, 489–492. <https://doi.org/10.1130/G22390.1>
- Evans, K.A. (2012) The redox budget of subduction zones. *Earth-Science Reviews* 113, 11–32. <https://doi.org/10.1016/j.earscirev.2012.03.003>
- Evans, K.A., Tomkins, A.G. (2011) The relationship between subduction zone redox budget and arc magma fertility. *Earth and Planetary Science Letters* 308, 401–409. <https://doi.org/10.1016/j.epsl.2011.06.009>
- Facq, S., Daniel, I., Montagnac, G., Cardon, H., Sverjensky, D.A. (2014) In situ Raman study and thermodynamic model of aqueous carbonate speciation in equilibrium with aragonite under subduction zone conditions. *Geochimica et Cosmochimica Acta* 132, 375–390. <https://doi.org/10.1016/j.gca.2014.01.030>
- Gaillard, F., Scaillet, B., Pichavant, M. (2002) Kinetics of iron oxidation-reduction in hydrous silicic melts. *American Mineralogist* 87, 829–837. <https://doi.org/10.2138/am-2002-0704>
- Helgeson, H.C., Kirkham, D.H., Flowers, G.C. (1981) Theoretical prediction of the thermodynamic behavior of aqueous electrolytes by high pressures and temperatures; IV, Calculation of activity coefficients, osmotic coefficients, and apparent molal and



- standard and relative partial molal properties to 600. *American Journal of Science*, 1249–1516. <https://doi.org/10.2475/ajs.281.10.1249>
- Hermann, J., Spandler, C., Hack, A., Korsakov, A.V. (2006) Aqueous fluids and hydrous melts in high-pressure and ultra-high pressure rocks: Implications for element transfer in subduction zones. *Lithos* 92, 399–417. <https://doi.org/10.1016/j.lithos.2006.03.055>
- Hermann, J., Spandler, C.J. (2008) Sediment melts at sub-arc depths: An experimental study. *Journal of Petrology* 49, 717–740. <https://doi.org/10.1093/petrology/egm073>
- Holland, T.J.B., Powell, R. (1998) An internally consistent thermodynamic data set for phases of petrological interest. *Journal of Metamorphic Geology* 16, 309–343. <https://doi.org/10.1111/j.1525-1314.1998.00140.x>
- Huang, F., Sverjensky, D.A. (2019) Extended Deep Earth Water Model for predicting major element mantle metasomatism. *Geochimica et Cosmochimica Acta* 254, 192–230. <https://doi.org/10.1016/j.gca.2019.03.027>
- Ionov, D.A., Bénard, A., Plechov, P.Y. (2011) Melt evolution in subarc mantle: Evidence from heating experiments on spinel-hosted melt inclusions in peridotite xenoliths from the andesitic Avacha volcano (Kamchatka, Russia). *Contributions to Mineralogy and Petrology* 162, 1159–1174. <https://doi.org/10.1007/s00410-011-0645-0>
- Kent, A.J.R., Peate, D.W., Newman, S., Stolper, E.M., Pearce, J.A. (2002) Chlorine in submarine glasses from the Lau Basin: Seawater contamination and constraints on the composition of slab-derived fluids. *Earth and Planetary Science Letters* 202, 361–377. [https://doi.org/10.1016/S0012-821X\(02\)00786-0](https://doi.org/10.1016/S0012-821X(02)00786-0)
- Klemme, S., O'Neill, H.S.C. (1997) The reaction $\text{MgCr}_2\text{O}_4 + \text{SiO}_2 = \text{Cr}_2\text{O}_3 + \text{MgSiO}_3$ and the free energy of formation of magnesiochromite (MgCr_2O_4). *Contributions to Mineralogy and Petrology* 130, 59–65. <https://doi.org/10.1007/s004100050349>
- Kress, V.C., Carmichael, I.S.E. (1991) The compressibility of silicate liquids containing Fe_2O_3 and the effect of composition, temperature, oxygen fugacity and pressure on their redox states. *Contributions to Mineralogy and Petrology* 108, 82–92. <https://doi.org/10.1007/BF00307328>
- Louvel, M., Sanchez-Valle, C., Malfait, W., Pokrovski, G., Borca, C., Grolimund, D. (2020) Bromine speciation and partitioning in slab-derived aqueous fluids and silicate melts and implications for halogens transfer in subduction zones. *Solid Earth* 11(4), 1145–1161. <https://doi.org/10.5194/se-11-1145-2020>
- Manning, C.E., Antignano, A., Lin, H.A. (2010) Premelting polymerization of crustal and mantle fluids, as indicated by the solubility of albite+paragonite+quartz in H_2O at 1 GPa and 350–620°C. *Earth and Planetary Science Letters* 292, 325–336. <https://doi.org/10.1016/j.epsl.2010.01.044>
- Marschall, H.R., Schumacher, J.C. (2012) Arc magmas sourced from mélange diapirs in subduction zones. *Nature Geoscience* 5, 862–867. <https://doi.org/10.1038/ngeo1634>
- Mysen, B.O. (2006) The structural behavior of ferric and ferrous iron in aluminosilicate glass near meta-aluminosilicate joins. *Geochimica et Cosmochimica Acta* 70, 2337–2353. <https://doi.org/10.1016/j.gca.2006.01.026>
- Newton, R.C., Manning, C.E. (2008) Thermodynamics of SiO_2 - H_2O fluid near the upper critical end point from quartz solubility measurements at 10 kbar. *Earth and Planetary Science Letters* 274, 241–249. <https://doi.org/10.1016/j.epsl.2008.07.028>
- Nielsen, S.G., Marschall, H.R. (2017) Geochemical evidence for mélange melting in global arcs. *Science Advances* 3, 1–7. <https://doi.org/10.1126/sciadv.1602402>
- Prescher, C., McCammon, C., Dubrovinsky, L. (2012) MossA: A program for analyzing energy-domain Mössbauer spectra from conventional and synchrotron sources. *Journal of Applied Crystallography* 45, 329–331. <https://doi.org/10.1107/S0021889812004979>
- Shock, E.L., Helgeson, H.C. (1988) Calculation of the thermodynamic and transport properties of aqueous species at high pressures and temperatures: Correlation algorithms for ionic species and equation of state predictions to 5 kb and 1000°C. *Geochimica et Cosmochimica Acta* 52, 2009–2036. [https://doi.org/10.1016/0016-7037\(88\)90181-0](https://doi.org/10.1016/0016-7037(88)90181-0)
- Shock, E.L., Helgeson, H.C. (1990) Calculation of the thermodynamic and transport properties of aqueous species at high pressures and temperatures: Standard partial molal properties of organic species. *Geochimica et Cosmochimica Acta* 54, 915–945. [https://doi.org/10.1016/0016-7037\(90\)90429-O](https://doi.org/10.1016/0016-7037(90)90429-O)
- Shock, E.L., Helgeson, H.C., Sverjensky, D.A. (1989) Calculation of the thermodynamic and transport properties of aqueous species



- at high pressures and temperatures: Standard partial molal properties of inorganic neutral species. *Geochimica et Cosmochimica Acta* 53, 2157–2183. [https://doi.org/10.1016/0016-7037\(89\)90341-4](https://doi.org/10.1016/0016-7037(89)90341-4)
- Shock, E.L., Sassani, D.C., Willis, M., Sverjensky, D.A. (1997) Inorganic species in geologic fluids: Correlations among standard molal thermodynamic properties of aqueous ions and hydroxide complexes. *Geochimica et Cosmochimica Acta* 61, 907–950. [https://doi.org/10.1016/S0016-7037\(96\)00339-0](https://doi.org/10.1016/S0016-7037(96)00339-0)
- Sverjensky, D.A. (2019) Thermodynamic modelling of fluids from surficial to mantle conditions. *Journal of the Geological Society* 176, 348–374. <https://doi.org/10.1144/jgs2018-105>
- Sverjensky, D.A., Harrison, B., Azzolini, D. (2014) Water in the deep Earth: The dielectric constant and the solubilities of quartz and corundum to 60kb and 1200°C. *Geochimica et Cosmochimica Acta* 129, 125–145. <https://doi.org/10.1016/j.gca.2013.12.019>
- Syracuse, E.M., van Keken, P.E., Abers, G.A. (2010) The global range of subduction zone thermal models. *Physics of the Earth and Planetary Interiors* 183, 73–90. <https://doi.org/10.1016/j.pepi.2010.02.004>
- Tanger, J.C., Helgeson, H.C. (1988) Calculation of the thermodynamic and transport properties of aqueous species at high pressures and temperatures; revised equations of state for the standard partial molal properties of ions and electrolytes. *American Journal of Science*, 19–98. <https://doi.org/10.2475/ajs.288.1.19>
- Tumiati, S., Godard, G., Martin, S., Malaspina, N., Poli, S. (2015) Ultra-oxidized rocks in subduction mélanges? Decoupling between oxygen fugacity and oxygen availability in a Mn-rich metasomatic environment. *Lithos* 226, 116–130. <https://doi.org/10.1016/j.lithos.2014.12.008>
- Van Keken, P.E., Hacker, B.R., Syracuse, E.M., Abers, G.A. (2011) Subduction factory: 4. Depth-dependent flux of H₂O from subducting slabs worldwide. *Journal of Geophysical Research: Solid Earth* 116. <https://doi.org/10.1029/2010JB007922>
- Wilke, M., Behrens, H., Burkhard, D.J.M., Rossano, S. (2002) The oxidation state of iron in silicic melt at 500 MPa water pressure. *Chemical Geology* 189, 55–67. [https://doi.org/10.1016/S0009-2541\(02\)00042-6](https://doi.org/10.1016/S0009-2541(02)00042-6)
- Wohlrs, A., Manning, C.E., Thompson, A.B. (2011). Experimental investigation of the solubility of albite and jadeite in H₂O, with paragonite + quartz at 500 and 600 C, and 1–2.25 GPa. *Geochimica et Cosmochimica Acta* 75, 2924–2939. <https://doi.org/10.1016/j.gca.2011.02.028>
- Wolery, T.J. (1992) EQ3NR, A Computer Program for Geochemical Aqueous Speciation-Solubility Calculations: Theoretical Manual, User's Guide, and Related Documentation (Version 7.0). 262. <https://doi.org/10.2172/138643>

